

ARTICLE

Open Access

Multi-dimensional band structure spectroscopy in the synthetic frequency dimension

Dali Cheng¹, Eran Lustig¹, Kai Wang^{1,2} and Shanhui Fan¹✉

Abstract

The concept of synthetic dimensions in photonics provides a versatile platform in exploring multi-dimensional physics. Many of these physics are characterized by band structures in more than one dimensions. Existing efforts on band structure measurements in the photonic synthetic frequency dimension however are limited to either one-dimensional Brillouin zones or one-dimensional subsets of multi-dimensional Brillouin zones. Here we theoretically propose and experimentally demonstrate a method to fully measure multi-dimensional band structures in the synthetic frequency dimension. We use a single photonic resonator under dynamical modulation to create a multi-dimensional synthetic frequency lattice. We show that the band structure of such a lattice over the entire multi-dimensional Brillouin zone can be measured by introducing a gauge potential into the lattice Hamiltonian. Using this method, we perform experimental measurements of two-dimensional band structures of a Hermitian and a non-Hermitian Hamiltonian. The measurements reveal some of the general properties of point-gap topology of the non-Hermitian Hamiltonian in more than one dimensions. Our results demonstrate experimental capabilities to fully characterize high-dimensional physical phenomena in the photonic synthetic frequency dimension.

Introduction

In the synthetic dimensions in photonics^{1–20}, different internal degrees of freedom of photons are coupled to form extra dimensions in addition to the dimensions of the real space. Using this concept, one can experimentally study novel physical phenomena unique to high-dimensional systems with low-dimensional platforms, which are of less complexity in engineering and control. Recent experimental accomplishments in photonic synthetic dimensions include the demonstration of photonic analogs of quantum Hall effect and topological insulators^{5,8,9,11,16}, as well as the realization of the skin effect and eigenvalue topologies in non-Hermitian systems^{21–23}.

In the experimental demonstration of many of these physical phenomena, band structure measurements are essential since much of the nontrivial physics of the

systems manifests in the band structure^{11,22–27}. In the synthetic frequency dimension⁷, current experimental band structure measurements are carried out in either the one-dimensional Brillouin zone^{11,22–25,27–29} or a one-dimensional subset of the two- or three-dimensional Brillouin zone³⁰. In this paper, we propose and demonstrate the method of multi-dimensional band structure spectroscopy in the synthetic frequency dimension. We demonstrate that the band structure over the entire multi-dimensional Brillouin zone can be probed, by exploiting a modulation phase which introduces a gauge potential in the Hamiltonian. As examples, we measure the two-dimensional band structures of both a Hermitian Hamiltonian and a non-Hermitian Hamiltonian. Our measurement reveals some of the general properties of point-gap topology of the non-Hermitian Hamiltonian in more than one dimensions. The results here demonstrate experimental capabilities to fully characterize high-dimensional physical phenomena in the photonic synthetic frequency dimension.

Correspondence: Shanhui Fan (shanhui@stanford.edu)

¹Ginzton Laboratory and Department of Electrical Engineering, Stanford University, Stanford, CA 94305, USA

²Department of Physics, McGill University, Montreal, QC H3A 2T8, Canada

© The Author(s) 2023



Open Access This article is licensed under a Creative Commons Attribution 4.0 International License, which permits use, sharing, adaptation, distribution and reproduction in any medium or format, as long as you give appropriate credit to the original author(s) and the source, provide a link to the Creative Commons license, and indicate if changes were made. The images or other third party material in this article are included in the article's Creative Commons license, unless indicated otherwise in a credit line to the material. If material is not included in the article's Creative Commons license and your intended use is not permitted by statutory regulation or exceeds the permitted use, you will need to obtain permission directly from the copyright holder. To view a copy of this license, visit <http://creativecommons.org/licenses/by/4.0/>.

Results

Theory of multi-dimensional Brillouin zone sampling

We here describe the theory of multi-dimensional band structure measurements in the synthetic frequency dimension. As an illustration we consider a Hamiltonian that describes a two-dimensional square lattice:

$$H = \frac{1}{2} \sum_{x,y} \left(g a_{x+1,y}^\dagger a_{x,y} + \kappa a_{x,y+1}^\dagger a_{x,y} + \text{H.c.} \right), \quad x, y \in \mathbb{Z} \tag{1}$$

Here, $a_{x,y}^\dagger$ and $a_{x,y}$ are creation and annihilation operators on the (x, y) lattice site, respectively. g and κ are real coupling constants along the x and y directions. The corresponding band structure is

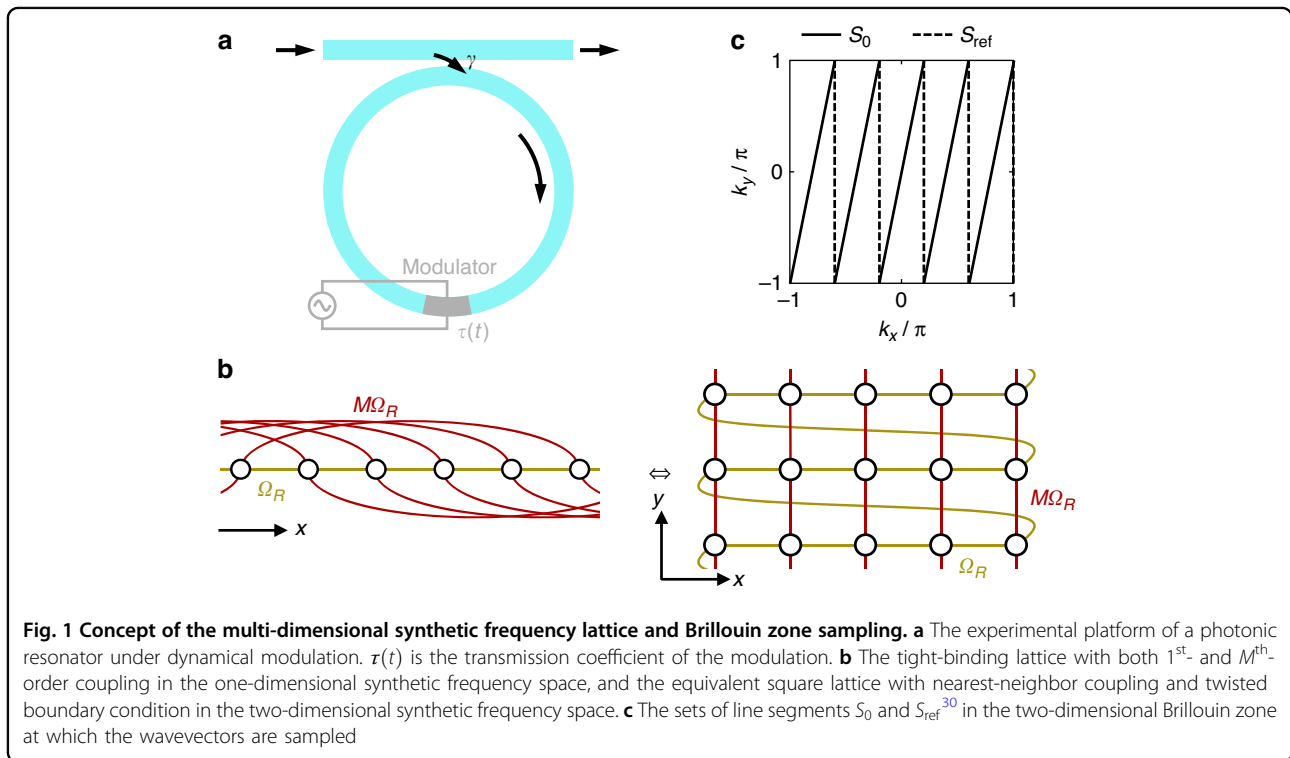
$$E(k_x, k_y) = g \cos k_x + \kappa \cos k_y \tag{2}$$

Strictly speaking, the band structure of Eq. (2) is applicable only when the lattice is of infinite size along both x and y directions, in which case the wavevectors k_x and k_y each occupies the entire interval of $(-\pi, \pi]$.

Our objective is to experimentally create and fully characterize multi-dimensional band structures such as Eq. (2) using the approach of synthetic frequency dimensions. We first review the approach to create and measure a one-dimensional band structure in the synthetic frequency dimension. As shown in Fig. 1a, one uses a photonic ring resonator under dynamical modulation.

The resonator by itself, without the modulation, supports a set of longitudinal modes that are equally spaced by the free spectral range $\Omega_R = 2\pi/T_R$, where T_R is the round-trip time of light propagation inside the resonator. Here we assume that both polarizations are degenerate in the resonator, that the group velocity dispersion is absent, and that the sizes of the modulators are negligible compared to the circumference of the resonator. When the resonator is modulated at Ω_R , resonator modes separated in frequency by Ω_R are coupled. Taking each mode as a lattice site, the dynamics of the mode amplitudes can be modeled by a one-dimensional tight-binding lattice along the synthetic frequency dimension⁷. To probe the band structure of this one-dimensional lattice, the resonator is excited by a continuous wave (CW) laser input with tunable frequency $\omega_{\text{CW}} = \omega_0 + n\Omega_R + \delta\omega$, through an input-output waveguide that couples to the ring with power coupling ratio γ . Here ω_0 is the central frequency, $n \in \mathbb{Z}$ and $\delta\omega$ is the frequency detuning. For each detuning $\delta\omega$, the light intensity ξ at an output port can be measured as a function of t , where $t \in (-T_R/2, T_R/2]$ is the time variable within each round-trip. By interpreting the time variable t as the wavevector k along the frequency axis, the band structure of this one-dimensional lattice can be extracted from the resonant features in the output intensity $\xi(\delta\omega, t)$ ²⁴.

Yuan et al. theoretically proposed that multi-dimensional Hamiltonians can also be synthesized using a single resonator as shown in Fig. 1a³¹. To implement the



Hamiltonian in Eq. (1), Yuan et al. considered a phase modulator with the transmission coefficient:

$$\tau_{\text{ref}}(t) = e^{i[gT_R \cos(\Omega_R t) + \kappa T_R \cos(M\Omega_R t)]} \quad (3)$$

Here $M > 1$ is an integer. Since the modulation waveform contains both Ω_R and $M\Omega_R$ frequency components, the m^{th} frequency mode in the resonator is coupled to both $(m \pm 1)^{\text{th}}$ mode and $(m \pm M)^{\text{th}}$ mode. The corresponding picture of a one-dimensional lattice in the synthetic frequency dimension is shown in Fig. 1b on the left, with $M = 5$. The 1st-order and M^{th} -order couplings are shown in brown and red, respectively. In this lattice, the M^{th} -order coupling can be viewed as the hopping along an additional synthetic frequency dimension. By rearranging the positions of the lattice sites, one can see that the one-dimensional lattice in Fig. 1b on the left is equivalent to a two-dimensional square lattice with nearest-neighbor coupling in Fig. 1b on the right. This square lattice is infinite along the y direction and has a finite size of M lattice sites along the x direction with a twisted boundary condition imposed on the edges^{14,31}. In this way, one can synthesize multi-dimensional lattices in a single resonator by additional modulation frequencies, although such lattices are in nature of finite size along all synthetic frequency dimensions except one.

In such multi-dimensional synthetic lattices with a twisted boundary condition as shown in Fig. 1b, the allowed wavevectors form a one-dimensional subset of the two-dimensional Brillouin zone of the corresponding infinite two-dimensional lattice. Consider an eigenstate $\psi(x, y)$ in the two-dimensional lattice in Fig. 1b on the right, with $1 \leq x \leq M$ and $x, y \in \mathbb{Z}$. We define the translation operators along x and y directions:

$$\begin{aligned} \hat{T}_x \psi(x, y) &= \begin{cases} \psi(x + 1, y), & x \neq M \\ \psi(1, y + 1), & x = M \end{cases} \\ \hat{T}_y \psi(x, y) &= \psi(x, y + 1) \end{aligned} \quad (4)$$

According to Bloch's Theorem, we can write $\psi(x, y + 1)$ in terms of $\psi(x, y)$ in two alternative ways: $\psi(x, y + 1) = \hat{T}_y \psi(x, y) = e^{ik_y} \psi(x, y)$, and $\psi(x, y + 1) = \hat{T}_x^M \psi(x, y) = e^{iMk_x} \psi(x, y)$. Here k_x and k_y are wavevectors along the x and y directions of the corresponding infinite two-dimensional lattice. Therefore $k_y = Mk_x \pmod{2\pi}$. In such a two-dimensional synthetic lattice under twisted boundary condition, the allowed wavevectors sample the first Brillouin zone of the corresponding infinite two-dimensional lattice at a set of line segments:

$$S_0 = \{(k_x, k_y) \mid k_y = Mk_x \pmod{2\pi}, -\pi < k_x, k_y \leq \pi\} \quad (5)$$

Thus, this twisted boundary condition does not affect the two-dimensional band structure except for discretizing the

allowed wavevectors. We notice that the multi-dimensional lattices proposed in ref.³¹ has been realized experimentally in ref.³⁰ with a large M on the order of 100. Ref.³⁰ provided results on the allowed wavevectors (dashed lines in Fig. 1c, S_{ref}) that differ from Eq. (5) (solid lines in Fig. 1c, S_0), but the differences vanish in the large- M limit. Our result here is applicable for any value of M .

As can be seen from Eq. (5) above, a key limitation of the existing scheme for multi-dimensional band structure measurements is that the high-dimensional Brillouin zone is not fully probed. Here we show that this limitation can be overcome by introducing a reconfigurable gauge potential into the Hamiltonian. As an illustration, to fully measure the band structure of Eq. (2) over the entire two-dimensional Brillouin zone, instead of Eq. (3), we set the transmission coefficient of the phase modulator as

$$\tau(t) = e^{iV(t)} = e^{i[gT_R \cos(\Omega_R t) + \kappa T_R \cos(M\Omega_R t + \varphi)]} \quad (6)$$

We show that the entire two-dimensional Brillouin zone can be fully sampled by varying both the time variable t and the modulation phase φ which operates as a gauge potential in the Hamiltonian³². In the weak-coupling limit $\gamma \ll 1$, the steady-state transmission function can be expressed as²³

$$\xi(\delta\omega, t) \approx 1 - 2\gamma \text{Re} \left\{ \frac{1}{e^{\gamma_0} e^{i[\delta\omega T_R - V(t)]} - 1} \right\} \quad (7)$$

where $\gamma_0 > 0$ represents the round-trip intrinsic loss of the resonator. The transmission function reaches minima when $\delta\omega T_R - V(t) = 0$, i.e.,

$$\delta\omega = g \cos(\Omega_R t) + \kappa \cos(M\Omega_R t + \varphi) \quad (8)$$

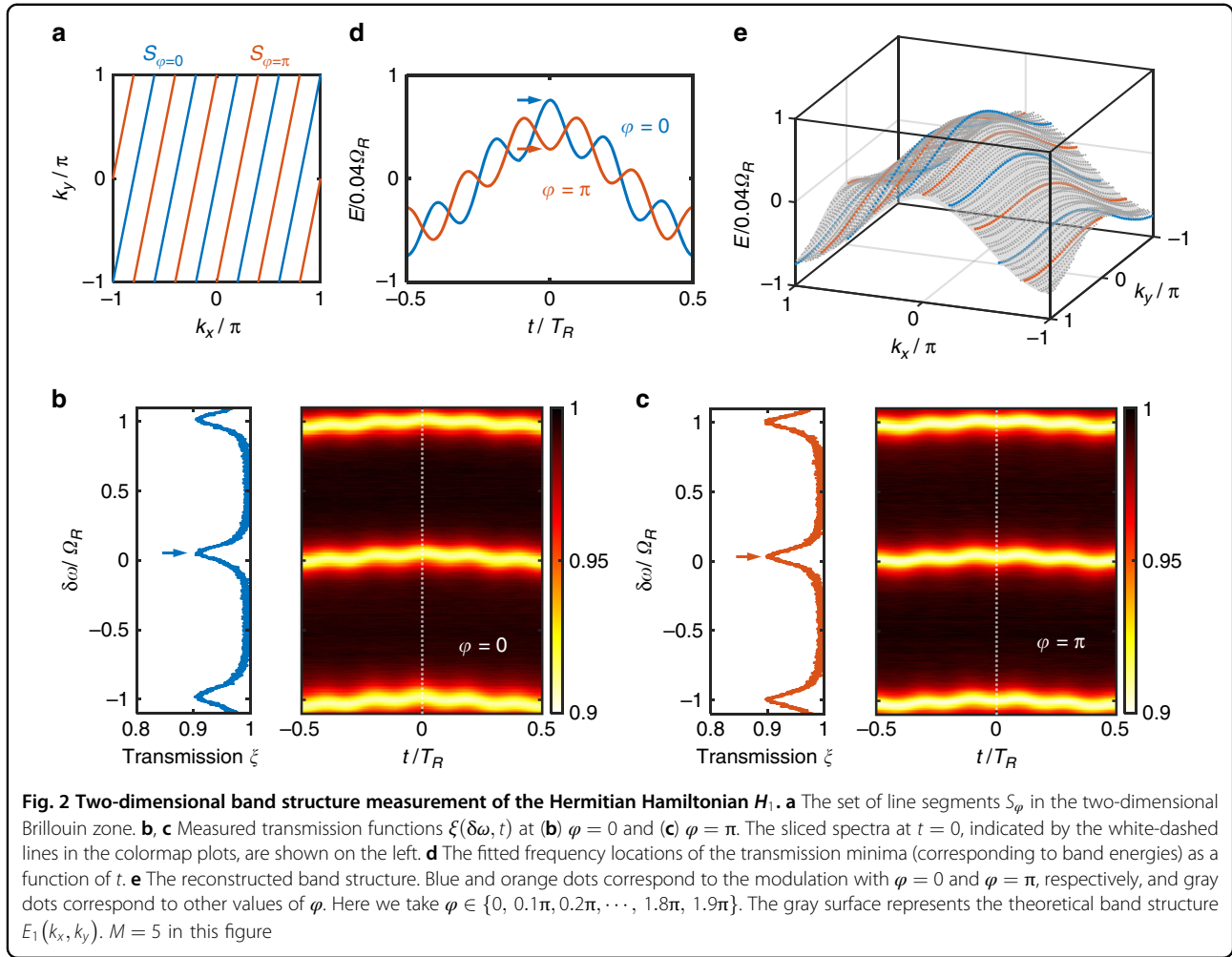
By comparing Eq. (2) and Eq. (8), we see that the locations of the minima of the transmission function correspond to the band energies $E(k_x, k_y)$, if we make the substitution

$$k_x = \Omega_R t, \quad k_y = M\Omega_R t + \varphi \pmod{2\pi} \quad (9)$$

By measuring the transmission function $\xi(\delta\omega, t)$, for a given φ , one probes the band structure at a set of line segments:

$$S_\varphi = \{(k_x, k_y) \mid k_y = Mk_x + \varphi \pmod{2\pi}, -\pi < k_x, k_y \leq \pi\} \quad (10)$$

Figure 2a shows in the Brillouin zone the sets S_φ with $M = 5$ and $\varphi = 0, \pi$. Note that S_0 is a special case of S_φ with $\varphi = 0$, as the gauge potential φ was not introduced in the derivation of Eq. (5). Since the modulation phase φ is a continuous variable that can be externally controlled, by continuously varying the values of φ over the range $[0, 2\pi)$



and by performing the time-dependent measurements as outlined above for each value of φ , we can reconstruct the band energy at every point in the Brillouin zone:

$$\bigcup_{\varphi \in [0, 2\pi)} S_\varphi = (-\pi, \pi] \otimes (-\pi, \pi] \quad (11)$$

Experimental measurement of a two-dimensional Hermitian band structure

Based on the theory above, here we provide an experimental demonstration of measurement of a two-dimensional Hermitian band structure in the synthetic frequency dimension. Our setup is similar to those in refs. 22–24. More detailed discussions can be found in the section of Materials and methods. The resonator is an optical fiber cavity with the free spectral range $\Omega_R = 2\pi \times 6\text{MHz}$. The resonator is excited by a narrow-linewidth continuous wave laser through a fiber coupler, and the laser frequency can be tuned within a range much larger than Ω_R . Inside the resonator, we incorporate lithium-niobate-based electro-optic modulators (EOMs),

and an erbium-doped fiber amplifier (EDFA) to partially compensate for the cavity loss. The light intensity ξ at the transmission port is measured by a large-bandwidth photodiode as a function of laser frequency and time.

Using the experimental setup, we perform band structure measurements on the two-dimensional lattice in Fig. 1b. Here we take $gT_R = 2\kappa T_R = 0.12$, and the band structure of our interest is $E_1(k_x, k_y) = 2\kappa \cos k_x + \kappa \cos k_y$. Based on the theory in the previous section, to synthesize and measure this band structure, we choose the transmission coefficient of the phase modulator as

$$\tau_1(t) = e^{i\kappa T_R [2 \cos(\Omega_R t) + \cos(M\Omega_R t + \varphi)]} \quad (12)$$

Given a specific value of φ , the measured transmission function $\xi(\delta\omega, t)$ reveals the band energies sampled at S_φ . By taking multiple measurements with different values of φ , we can characterize the two-dimensional band structure $E_1(k_x, k_y)$ over the entire first Brillouin zone in two dimensions.

The right panels in Fig. 2b, c show the transmission function $\xi(\delta\omega, t)$ at $\varphi = 0$ and $\varphi = \pi$, respectively. The left panels show the corresponding line plots for $\xi(\delta\omega, t = 0)$. At each t , the transmission function exhibits a periodic set of resonant features, and the frequency difference between the neighboring transmission minima is Ω_R . The periodic behavior here arises from the translational symmetry of the lattice in Fig. 1b along the synthetic frequency dimension. Figure 2d shows the frequency locations of the transmission minima as a function of t for $\varphi = 0$ and $\varphi = \pi$. We see that these locations shift as φ varies. These locations, as mentioned above, correspond to the band energy $E_1(k_x, k_y)$ sampled at S_φ . In Fig. 2e, we reconstruct the measured band structure in the two-dimensional Brillouin zone according to Eq. (10). The measured band structure agrees well with the theoretical value represented by the gray surface.

Experimental measurement of a two-dimensional non-Hermitian band structure and its point-gap topology

We now use the capability, as demonstrated above, to explore novel topological features of non-Hermitian band structures in two dimensions. Non-Hermitian systems can manifest many intriguing properties that have no counterparts in Hermitian systems^{33–41}. A key novel aspect of the non-Hermitian band structure is that the eigenvalues, being complex, exhibit nontrivial topology in the wavevector space^{42–45}. In one-dimension, non-Hermitian systems can exhibit point-gap topology where the eigenvalues form nontrivial contours as the wavevector varies across the first Brillouin zone. This point-gap topology was first experimentally demonstrated in the synthetic frequency dimension in²², and is related to the non-Hermitian skin effect^{44,46–48} when the lattice is truncated due to the bulk-boundary correspondence. It was also noted theoretically that such point-gap topology can also exist in higher dimensional systems^{49–53}, with additional constraints due to the geometry of the Brillouin zone. Here we provide an experimental demonstration of point-gap topology in two-dimensional systems which has not been previously carried out.

We consider the non-Hermitian Hamiltonian

$$H_2 = \frac{\mu+i\eta}{2} \sum_{x,y} \left(a_{x+1,y}^\dagger a_{x,y} + a_{x-1,y}^\dagger a_{x,y} \right) + \frac{\mu-i\eta}{2} \sum_{x,y} \left(a_{x,y+1}^\dagger a_{x,y} + a_{x,y-1}^\dagger a_{x,y} \right), \quad x, y \in \mathbb{Z} \tag{13}$$

where μ, η are real coupling constants. This Hamiltonian is described by a complex symmetric matrix and hence is reciprocal. This Hamiltonian also has the $\mathcal{R}\mathcal{T}$ symmetry, where \mathcal{R} is the reflection operation against the line $x = y$, and \mathcal{T} is the time-reversal operation. The band structure

of this Hamiltonian is

$$E_2(k_x, k_y) = \mu(\cos k_x + \cos k_y) + i\eta(\cos k_x - \cos k_y) \tag{14}$$

Such band structure can exhibit nontrivial point-gap topology. In the two-dimensional Brillouin zone, we define a set of line segments

$$L(\alpha, \delta k) = \{ (k_x, k_y) \mid k_y = \alpha k_x + \delta k \pmod{2\pi}, \alpha \in \mathbb{Q} \cup \{\infty\}, \delta k \in \mathbb{R}, -\pi < k_x, k_y \leq \pi \} \tag{15}$$

where α is the direction (slope) of the line segments and is assumed to be a rational number. These line segments are connected at the edges of the Brillouin zone, and topologically, $L(\alpha, \delta k)$ forms a closed loop in the two-dimensional Brillouin zone \mathbb{T}^2 . Associated with $L(\alpha, \delta k)$ we can define the winding number^{43,51}

$$w(L(\alpha, \delta k), E_0) \equiv \frac{1}{2\pi i} \oint_{L(\alpha, \delta k)} dk \frac{\partial}{\partial k} \log[E_2(k) - E_0] \tag{16}$$

where $E_0 \in \mathbb{C}$ is the reference energy. A non-zero winding number indicates a nontrivial point-gap topology along the loop.

As was noted in refs. 51,52, in high dimensions there are general theoretical results about these winding numbers, depending on the nature of the loops. For a reciprocal Hamiltonian, its band structure satisfies $E(-k_x, -k_y) = E(k_x, k_y)$, and therefore

$$w(L, E_0) = -w(\tilde{L}, E_0) \tag{17}$$

where \tilde{L} is the time-reversal partner of L . And for a time-reversal invariant loop with $L = \tilde{L}$, the winding number is zero. The aim of our experiments in this section is to demonstrate these theoretical observations.

To implement the non-Hermitian band structure $E_2(k_x, k_y)$, we incorporate both phase and amplitude modulations in the resonator. The transmission coefficients of the modulators are

$$\begin{aligned} \tau_2^{\text{phs}}(t) &= e^{i\mu T_R [\cos(\Omega_R t) + \cos(M\Omega_R t + \varphi)]}, \\ \tau_2^{\text{amp}}(t) &= e^{-\eta T_R [\cos(\Omega_R t) - \cos(M\Omega_R t + \varphi)]} \end{aligned} \tag{18}$$

where $\mu T_R = 0.09$ and $\eta T_R = 0.08$. With different values of φ , we take multiple measurements of the transmission function $\xi(\delta\omega, t)$ to reconstruct $E_2(k_x, k_y)$. Note that the imaginary part of the band energy is associated with the linewidth of the resonant features in the spectrum $\xi(\delta\omega, t)$ for a given t ²².

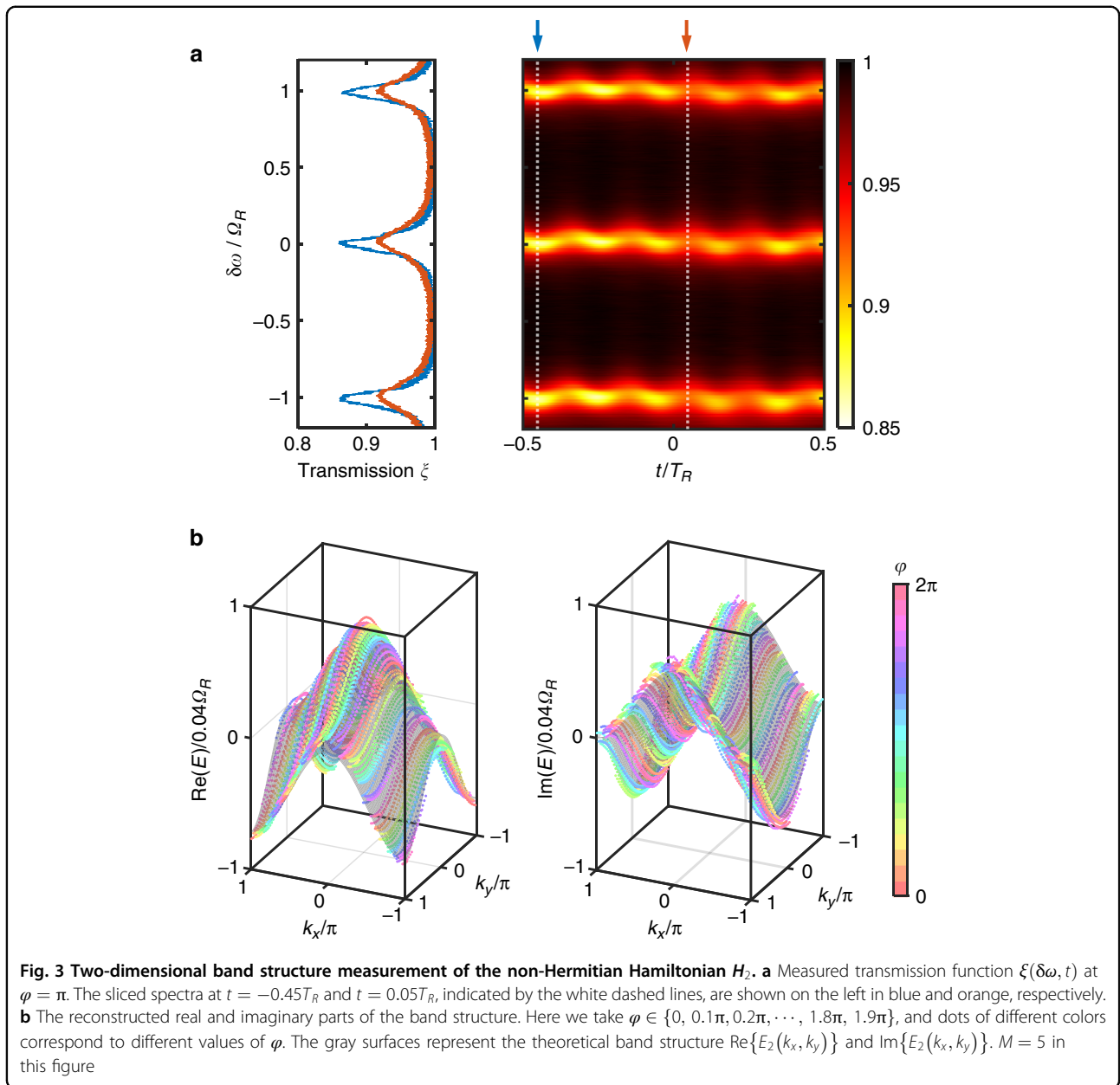


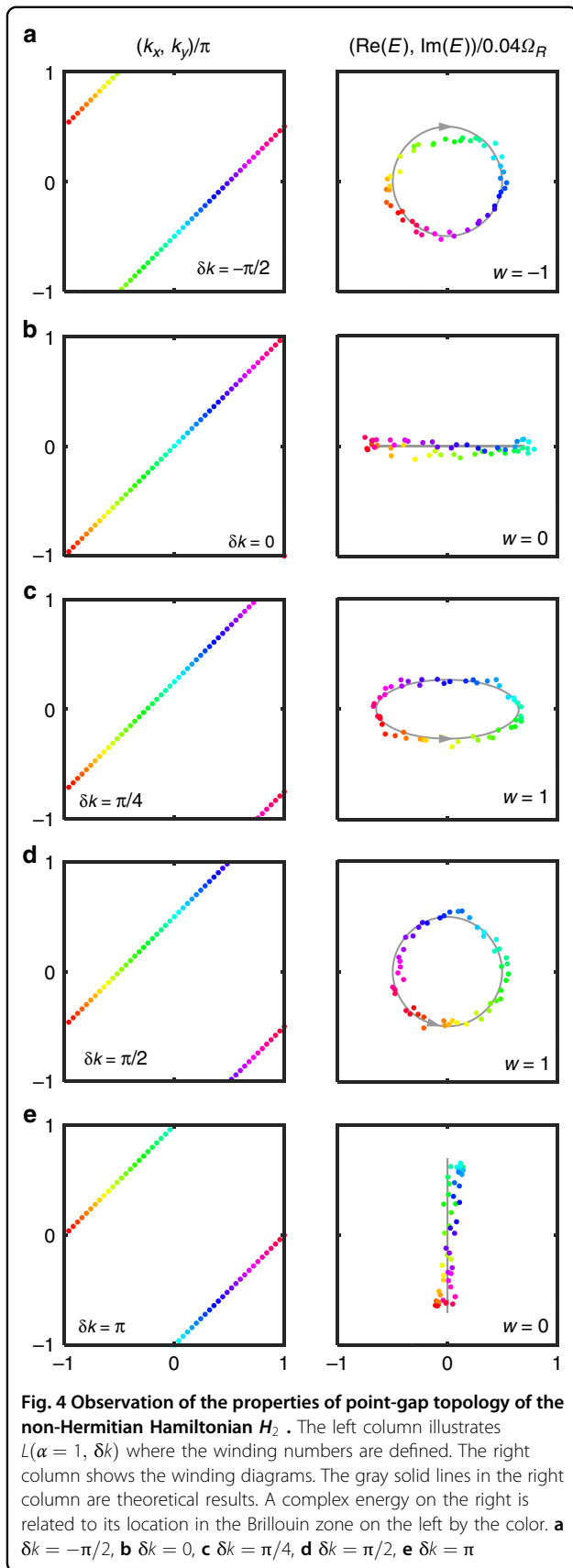
Figure 3 presents the measured band structure with the modulation Eq. (18). Figure 3a shows the transmission function with $\varphi = \pi$, with $\xi(\delta\omega, t = -0.45T_R)$ and $\xi(\delta\omega, t = 0.05T_R)$ displayed on the left as examples. With dynamic amplitude modulation, the instantaneous loss rate inside the resonator is not a constant, and in this example the spectrum $\xi(\delta\omega, t = -0.45T_R)$ has a sharper line shape than $\xi(\delta\omega, t = 0.05T_R)$. By extracting the locations and linewidths of the resonant features as a function of t , we obtain $\text{Re}(E_2)$ and $\text{Im}(E_2)$ along the set of line segments S_φ in the two-dimensional Brillouin zone. In Fig. 3b, we plot the real and imaginary parts of the reconstructed band structure $E_2(k_x, k_y)$, in agreement

with the theoretical values represented by the gray surfaces.

To demonstrate Eq. (17), we choose the loop L described by $E_0 = 0$ and $\alpha = 1$ in Eq. (16). Here we write $w(L(\alpha = 1, \delta k), E_0 = 0)$ as $w(\delta k)$ for convenience. From Eq. (17) we have

$$w(-\delta k) = -w(\delta k) \tag{19}$$

And for time-reversal invariant loops, i.e., $\delta k = 0$ or $\delta k = \pi$, the winding number is zero. In Fig. 4, we demonstrate the winding property stated by Eq. (19). For a given δk , we extract from Fig. 3b the complex energy at each point



along the loop $L(\alpha = 1, \delta k)$, and the trajectory of the complex energies form the winding diagram. In Fig. 4, we notice that when $\delta k = 0$ or $\delta k = \pi$, the complex energies lie on a line and thus the winding number is indeed zero. For other values of δk , the winding is nontrivial. In particular, for $\delta k = -\pi/2$ and $\delta k = \pi/2$, the windings are of the same geometric shape but in opposite directions. This agrees with Eq. (19). In fact, for this Hamiltonian H_2 , we always have $w(\delta k) = 1$ when $0 < \delta k < \pi$, and $w(\delta k) = -1$ when $-\pi < \delta k < 0$.

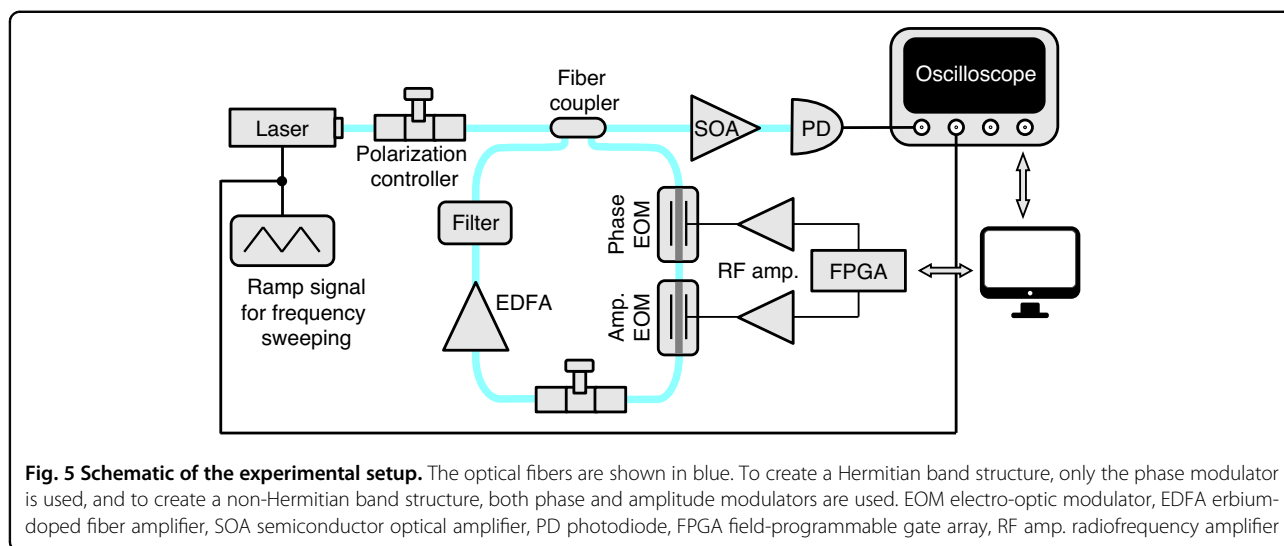
Discussion

In this paper, we have proposed and demonstrated the method of multi-dimensional band structure spectroscopy in the photonic synthetic frequency dimension. By varying the modulation phase, we can fully reconstruct the band structure at each point in the multi-dimensional Brillouin zone. As examples, we create and fully characterize the band structures of both a Hermitian and a non-Hermitian tight-binding Hamiltonian on two-dimensional square lattices. We also observe some of the general properties of point-gap topology of the non-Hermitian Hamiltonian in more than one dimensions. To generalize the method to three- or higher-dimensional systems, one can incorporate more frequency components in the modulation signal. By tuning the gauge potential associated with each frequency component, the entire high-dimensional Brillouin zone can be accessible. Our method can also be applied to models of more complexity, for example, models with multiple bands in higher dimensions and with more complicated connectivity between the lattice sites.

Materials and methods

Experimental setup

The schematic of our experimental platform is shown in Fig. 5. The setup is based on optical fibers. The resonator has a free spectral range of $\Omega_R = 2\pi \times 6\text{MHz}$. Our light source is a grade 3 Orion laser from Redfern integrated optics, a continuous wave laser in the telecommunication C-band with a center wavelength of 1542.057 nm and a linewidth of 2.8 kHz. The frequency of the laser is tunable and controlled by a function generator, which generates a ramp voltage signal of 600 mV_{pp} amplitude and 100 Hz frequency. The laser frequency is thus swept in a range of approximately $13\Omega_R$. The coupling between the input-output waveguide and the resonator is implemented by a 2×2 fiber coupler (beam splitter) of 95:5 power coupling ratio. Inside the resonator, light goes through phase and amplitude modulators, a polarization controller, an erbium-doped fiber amplifier (EDFA), and a dense wavelength-division multiplexing (DWDM) band-pass filter. The modulators are based on the electro-optic modulation in lithium niobate waveguides. The



modulation signals are generated by Red Pitaya STEMLab field-programmable gate arrays (FPGAs) with 60 mV_{pp} amplitude, and then amplified by Mini-Circuits ZHL-3A+ coaxial radiofrequency (RF) amplifiers and applied to the modulators. The polarization controller ensures that the light polarization remains unchanged after one round-trip propagation inside the resonator. The EDFA is used to partially compensate for the intrinsic loss in the resonator. We use a lower gain in the experiment to avoid gain saturation of the EDFA and lasing of the cavity. The band-pass filter, in channel 44, has a center wavelength of 1542.14 nm and a bandwidth of 26.5 GHz. It is used to suppress the amplified spontaneous emission noise of the EDFA, and supports $\sim 4.4 \times 10^3$ frequency modes in its transmission bandwidth. Finally, light at the transmission port is pre-amplified by a semiconductor optical amplifier (SOA) to improve the signal-to-noise ratio, and then detected by a photodiode (PD) with 5 GHz bandwidth. The detected signal is collected by an oscilloscope with a sampling rate of 2 GSa/s.

Data processing

The transmission function $\xi(\delta\omega, t)$ is dependent on both the laser detuning $\delta\omega$ and the time variable t . By making $\delta\omega$ linearly dependent on time, we can obtain the entire $\xi(\delta\omega, t)$ function within a single-shot measurement²⁴ where we sweep the laser frequency by a ramp signal. When processing the detected signal from the oscilloscope, we sequentially truncate the temporal signal into time intervals of length T_R . We assume that the laser frequency is unchanged within each time interval, but is different for different time intervals. Such approximation is valid since the laser frequency only changes by $2 \times 10^{-4} \Omega_R$ between neighboring time intervals. In Figs. 2 and 3, for each φ we take a measurement of $\xi(\delta\omega, t)$.

Given a time t , we use the Lorentzian line shape to fit the spectrum ξ as a function of $\delta\omega$, and obtain the locations of the transmission minima and the linewidth²². The intrinsic loss γ_0 of the resonator contributes to the fitted linewidth, and is removed as a background constant when calculating the imaginary part of the band structure. We also take into consideration the delay times that the RF signals propagate from the output ports of the FPGA to the input ports of the modulators, and the frequency-dependent phase responses of the RF amplifiers.

Acknowledgements

We thank Professor David A. B. Miller for providing laboratory space and equipment. This work is supported by MURI projects from the U.S. Air Force Office of Scientific Research (Grants No. FA9550-18-1-0379 and FA9550-22-1-0339).

Author contributions

D.C., E.L., K.W., and S.F. conceived the idea. D.C. and K.W. did the experiments. D.C. and S.F. wrote the manuscript. S.F. supervised the research.

Conflict of interest

The authors declare no competing interests.

Received: 21 March 2023 Revised: 23 May 2023 Accepted: 26 May 2023
Published online: 27 June 2023

References

- Boada, O. et al. Quantum simulation of an extra dimension. *Phys. Rev. Lett.* **108**, 133001 (2012).
- Ozawa, T. et al. Synthetic dimensions in integrated photonics: from optical isolation to four-dimensional quantum Hall physics. *Phys. Rev. A* **93**, 043827 (2016).
- Luo, X. W. et al. Synthetic-lattice enabled all-optical devices based on orbital angular momentum of light. *Nat. Commun.* **8**, 16097 (2017).
- Bell, B. A. et al. Spectral photonic lattices with complex long-range coupling. *Optica* **4**, 1433–1436 (2017).
- Zilberberg, O. et al. Photonic topological boundary pumping as a probe of 4D quantum Hall physics. *Nature* **553**, 59–62 (2018).

6. Qin, C. Z. et al. Spectrum control through discrete frequency diffraction in the presence of photonic gauge potentials. *Phys. Rev. Lett.* **120**, 133901 (2018).
7. Yuan, L. Q. et al. Synthetic dimension in photonics. *Optica* **5**, 1396–1405 (2018).
8. Lustig, E. et al. Photonic topological insulator in synthetic dimensions. *Nature* **567**, 356–360 (2019).
9. Ozawa, T. & Price, H. M. Topological quantum matter in synthetic dimensions. *Nature Rev. Phys.* **1**, 349–357 (2019).
10. Chalabi, H. et al. Synthetic gauge field for two-dimensional time-multiplexed quantum random walks. *Phys. Rev. Lett.* **123**, 150503 (2019).
11. Dutt, A. et al. A single photonic cavity with two independent physical synthetic dimensions. *Science* **367**, 59–64 (2020).
12. Chalabi, H. et al. Guiding and confining of light in a two-dimensional synthetic space using electric fields. *Optica* **7**, 506–513 (2020).
13. Dutt, A. et al. Higher-order topological insulators in synthetic dimensions. *Light Sci. Appl.* **9**, 131 (2020).
14. Wang, K. et al. Multidimensional synthetic chiral-tube lattices via nonlinear frequency conversion. *Light Sci. Appl.* **9**, 132 (2020).
15. Hu, Y. W. et al. Realization of high-dimensional frequency crystals in electro-optic microcombs. *Optica* **7**, 1189–1194 (2020).
16. Lustig, E. & Segev, M. Topological photonics in synthetic dimensions. *Adv. Opt. Photon.* **13**, 426–461 (2021).
17. Cheng, D. L. et al. Arbitrary synthetic dimensions via multiboson dynamics on a one-dimensional lattice. *Phys. Rev. Res.* **3**, 033069 (2021).
18. Leefmans, C. et al. Topological dissipation in a time-multiplexed photonic resonator network. *Nat. Phys.* **18**, 442–449 (2022).
19. Hu, Y. W. et al. Mirror-induced reflection in the frequency domain. *Nat. Commun.* **13**, 6293 (2022).
20. Cheng, D. L., Wang, K. & Fan, S. H. Artificial non-Abelian lattice gauge fields for photons in the synthetic frequency dimension. *Phys. Rev. Lett.* **130**, 083601 (2023).
21. Weidemann, S. et al. Topological funneling of light. *Science* **368**, 311–314 (2020).
22. Wang, K. et al. Generating arbitrary topological windings of a non-Hermitian band. *Science* **371**, 1240–1245 (2021).
23. Wang, K. et al. Topological complex-energy braiding of non-Hermitian bands. *Nature* **598**, 59–64 (2021).
24. Dutt, A. et al. Experimental band structure spectroscopy along a synthetic dimension. *Nat. Commun.* **10**, 3122 (2019).
25. Li, G. Z. et al. Dynamic band structure measurement in the synthetic space. *Sci. Adv.* **7**, eabe4335 (2021).
26. Yang, M. et al. Topological band structure via twisted photons in a degenerate cavity. *Nat. Commun.* **13**, 2040 (2022).
27. Li, G. Z. et al. Direct extraction of topological Zak phase with the synthetic dimension. *Light Sci. Appl.* **12**, 81 (2023).
28. Balčytis, A. et al. Synthetic dimension band structures on a Si CMOS photonic platform. *Sci. Adv.* **8**, eabk0468 (2022).
29. Dutt, A. et al. Creating boundaries along a synthetic frequency dimension. *Nat. Commun.* **13**, 3377 (2022).
30. Senanian, A. et al. Programmable large-scale simulation of bosonic transport in optical synthetic frequency lattices. *Nat. Phys.* (2023).
31. Yuan, L. Q. et al. Synthetic space with arbitrary dimensions in a few rings undergoing dynamic modulation. *Phys. Rev. B* **97**, 104105 (2018).
32. Fang, K. J., Yu, Z. F. & Fan, S. H. Realizing effective magnetic field for photons by controlling the phase of dynamic modulation. *Nat. Photon.* **6**, 782–787 (2012).
33. Bender, C. M. et al. Faster than Hermitian quantum mechanics. *Phys. Rev. Lett.* **98**, 040403 (2007).
34. Barreiro, J. T. et al. An open-system quantum simulator with trapped ions. *Nature* **470**, 486–491 (2011).
35. Zheng, C., Hao, L. & Long, G. L. Observation of a fast evolution in a parity-time-symmetric system. *Philos. Trans. R. Soc. A: Math. Phys. Eng. Sci.* **371**, 20120053 (2013).
36. Sergi, A. & Zloshchastiev, K. G. Quantum entropy of systems described by non-Hermitian Hamiltonians. *J. Stat. Mech. TheoryExp.* **2016**, 033102 (2016).
37. Wen, J. W. et al. Observation of information flow in the anti-*PT*-symmetric system with nuclear spins. *npj Quant. Inf.* **6**, 28 (2020).
38. Del Re, L. et al. Driven-dissipative quantum mechanics on a lattice: simulating a fermionic reservoir on a quantum computer. *Phys. Rev. B* **102**, 125112 (2020).
39. Zheng, C. Universal quantum simulation of single-qubit nonunitary operators using duality quantum algorithm. *Sci. Rep.* **11**, 3960 (2021).
40. Li, D. L. & Zheng, C. Non-Hermitian generalization of Rényi entropy. *Entropy* **24**, 1563 (2022).
41. Wu, C., Fan, A. N. & Liang, S. D. Complex Berry curvature and complex energy band structures in non-Hermitian graphene model. *AAPPS Bull.* **32**, 39 (2022).
42. Shen, H. T., Zhen, B. & Fu, L. Topological band theory for non-Hermitian Hamiltonians. *Phys. Rev. Lett.* **120**, 146402 (2018).
43. Gong, Z. P. et al. Topological phases of non-Hermitian systems. *Phys. Rev. X* **8**, 031079 (2018).
44. Okuma, N. et al. Topological origin of non-Hermitian skin effects. *Phys. Rev. Lett.* **124**, 086801 (2020).
45. Bergholtz, E. J., Budich, J. C. & Kunst, F. K. Exceptional topology of non-Hermitian systems. *Rev. Mod. Phys.* **93**, 015005 (2021).
46. Lee, T. E. Anomalous edge state in a non-Hermitian lattice. *Phys. Rev. Lett.* **116**, 133903 (2016).
47. Yao, S. Y. & Wang, Z. Edge states and topological invariants of non-Hermitian systems. *Phys. Rev. Lett.* **121**, 086803 (2018).
48. Zhang, K., Yang, Z. S. & Fang, C. Correspondence between winding numbers and skin modes in non-Hermitian systems. *Phys. Rev. Lett.* **125**, 126402 (2020).
49. Liu, T. et al. Second-order topological phases in non-Hermitian systems. *Phys. Rev. Lett.* **122**, 076801 (2019).
50. Kawabata, K., Sato, M. & Shiozaki, K. Higher-order non-Hermitian skin effect. *Phys. Rev. B* **102**, 205118 (2020).
51. Zhong, J. et al. Nontrivial point-gap topology and non-Hermitian skin effect in photonic crystals. *Phys. Rev. B* **104**, 125416 (2021).
52. Zhang, K., Yang, Z. S. & Fang, C. Universal non-Hermitian skin effect in two and higher dimensions. *Nat. Commun.* **13**, 2496 (2022).
53. Wojcik, C. C. et al. Eigenvalue topology of non-Hermitian band structures in two and three dimensions. *Phys. Rev. B* **106**, L161401 (2022).